

Interplay of Coulomb and nonparabolicity effects in the intersubband absorption of electrons and holes in quantum wells

M. F. Pereira, Jr.

NMRC, University College Cork, Lee Maltings, Prospect Row, Cork, Ireland

H. Wenzel

Ferdinand-Braun Institut für Höchstfrequenztechnik, Gustav-Kirchhoff-Strasse 4, D-12489 Berlin, Germany

(Received 6 April 2004; revised manuscript received 20 August 2004; published 22 November 2004)

Quantum well intersubband absorption with contributions from both valence and conduction subbands is computed with a nonequilibrium Keldysh Green's function formalism, assuming an optical pump and probe scheme in undoped samples. The coupling between conduction and valence bands leads to contributions to the TE mode from the electrons, which are enhanced due to Coulomb corrections and may be resolved even in the presence of the dominating hole contributions. A strong contrast in the evolution of absorption spectra with increasing carrier density is predicted between TM and TE polarizations. The influence of strongly k -dependent dipole moments in combination with many-body effects is analyzed for intersubband transitions, including the evolution of the spectra with increasing excitation power. For the TE case, extra features appear in the spectra, due to interplays between band structure and Coulomb effects which are not present in the TM mode. The spectral evolution on both polarizations, broadening, number, and relative strength of the resolved peaks are in strong contrast with free-carrier results. Numerical results are given for four different structures.

DOI: 10.1103/PhysRevB.70.205331

PACS number(s): 71.10.-w, 73.21.Fg, 78.67.De

I. INTRODUCTION

Many-body effects are crucial for a consistent explanation of conduction intersubband absorption of quantum wells (QW's), a fact that has been demonstrated by detailed comparisons between theory and experiments.¹⁻⁴ Typical interconduction subband transitions can be described with parabolic dispersion relations and constant dipole moments.^{5,6} In contrast, intervalence-band transitions are characterized by strong nonparabolicity and k -dependent dipole moments.^{7,8}

In this paper, we address the following issues: (i) intervalence subband contributions to the absorption have been studied for free carriers,⁷⁻⁹ and thus, in view of importance of Coulomb effects, we analyze the valence subband problem. We find that the strong band coupling and resulting nonparabolicity and k dependence of the dipole moments combined with Coulomb corrections lead to double features in some of the multiple transitions, which are directly measurable by comparing and contrasting the evolution of the TE and TM modes with increasing excitation. The spectra are radically different from free-carrier calculations.

(ii) The combined contributions from both types of subbands to the intersubband transitions including many-body effects and nonparabolicity in all subbands are discussed. That is possible by introducing a predictive numerical scheme capable of simulating experiments similar to those described in, e.g., Refs. 10,11, i.e., we assume a pump and probe excitation scheme, with a strong pump pulse generating electrons in the conduction band and holes in the valence bands, and a weak probe pulse in the infrared.

(iii) The conduction band states are a mix of electrons and holes, thus conduction band signatures are predicted in the TE mode even in the presence of the larger hole contribution due to a hitherto unexplored Coulomb enhancement of the

strongly nonparabolic conduction bands. The spectral positions and broadening, number of peaks, and the relative oscillator strengths of the spectra calculated with and without Coulomb effects are radically different, further highlighting the importance of our calculations.

II. MAIN EQUATIONS

Optical absorption α at a given photon energy $\hbar\omega$ can be calculated from the imaginary part of the optical susceptibility,

$$\alpha(\omega) = \frac{4\pi\omega}{cn_b} \mathcal{I}\{\chi(\omega)\}, \quad \chi(\omega) = 2 \sum_{\mu \neq \nu, k} d_{\mu\nu} \chi_{\nu,\mu}(k, \omega). \quad (1)$$

Here n_b denotes the background refractive index, c is the speed of light, $d_{\nu\mu}$ is the transition dipole moment between the subbands ν and μ , which are labeled $\mu=1,2,\dots$ from the top valence band. Thus in the discussion of numerical results that follows, absorption of light with an electron being promoted between, e.g., conduction subband $\mu=1$ to $\nu=2$ is called a (1,2) transition, while absorption with an electron being promoted, e.g., from valence subband $\mu=3$ to $\nu=2$ is called a (3,2) transition.

By running over all subband indices $\nu \neq \mu$ in Eqs. (1), we do not apply the rotating wave approximation.

The susceptibility function, $\chi_{\nu,\mu}(k, \omega)$ is related to the carrier Keldysh nonequilibrium Green's function, G . Its time evolution is described by a Dyson equation, with Coulomb interactions as well as other scattering mechanisms included in a self-energy, Σ .^{12,13}

The carrier self-energy includes scattering and leads to intersubband renormalization and spectral broadening, as well as exchange and depolarization effects.

The steady-state absorption spectra discussed have been numerically computed assuming the carriers are thermalized in quasiequilibrium in the various subbands, each subband “ λ ” characterized by the occupation function $f_\lambda(k)$. We do not use the electron-hole picture, and thus our notation is valid for both conduction and valence band electrons and occupation functions. The resulting integral equation for the susceptibility function reads

$$\begin{aligned} & [\hbar\omega - e_{\nu\mu}(\mathbf{k}) + i\Gamma_{\nu\mu}] \chi_{\nu\mu}(\mathbf{k}, \omega) - \delta f_{\nu\mu}(\mathbf{k}) \sum_{\mathbf{k}' \neq \mathbf{k}} \chi_{\nu\mu}(\mathbf{k}', \omega) \\ & \times \left(V \begin{pmatrix} \nu\nu\mu\mu \\ \mathbf{k} - \mathbf{k}' \end{pmatrix} - 2V \begin{pmatrix} \nu\mu\mu\nu \\ 0 \end{pmatrix} \right) = d_{\nu\mu} \delta f_{\nu\mu}(\mathbf{k}). \end{aligned} \quad (2)$$

The population difference is given by $\delta f_{\nu\mu}(\mathbf{k}) = f_\nu(\mathbf{k}) - f_\mu(\mathbf{k})$, the bare Coulomb interaction matrix elements read

$$\begin{aligned} V \begin{pmatrix} \mu\nu\lambda\beta \\ \mathbf{k} - \mathbf{k}' \end{pmatrix} &= \int dz dz' \phi_\mu^*(z) \phi_\nu(z) \\ & \times \frac{2\pi e^2 \exp(-|\mathbf{k} - \mathbf{k}'||z - z'|)}{\epsilon_0 A |\mathbf{k} - \mathbf{k}'|} \phi_\lambda^*(z') \phi_\beta(z'), \end{aligned} \quad (3)$$

where A , and ϵ_0 denote, respectively, a normalization area, and the background dielectric constant,

$$\begin{aligned} e_{\nu\mu}(\mathbf{k}) &= E_\nu(\mathbf{k}) - E_\mu(\mathbf{k}) - \sum_{\mathbf{k}'} f_\nu(\mathbf{k}') V \begin{pmatrix} \nu\nu\nu\nu \\ \mathbf{k} - \mathbf{k}' \end{pmatrix} \\ & + \sum_{\mathbf{k}'} f_\mu(\mathbf{k}') V \begin{pmatrix} \mu\mu\mu\mu \\ \mathbf{k} - \mathbf{k}' \end{pmatrix} \\ & + \sum_{\mathbf{k}'} [f_\nu(\mathbf{k}') - f_\mu(\mathbf{k}')] V \begin{pmatrix} \nu\mu\mu\nu \\ \mathbf{k} - \mathbf{k}' \end{pmatrix}, \end{aligned} \quad (4)$$

is the energy difference between the levels renormalized by the exchange interaction, which we refer to as the subband shift in the following. The calculated broadening, $\Gamma_{\nu\mu}$, is due to electron-electron scattering. More details are given in the Appendix.

The first term in brackets on the left-hand side of Eq. (2) (exchange) is analogous to the excitonic coupling term in interband transitions, while the second term gives rise to the depolarization shift, which leads to a dynamic renormalization.

In Eq. (2) we do not consider summations over all possible subband index, or in other words, we do not consider Coulomb couplings between different subbands, in order to reduce the size of the matrix to be inverted numerically as discussed below. A more complete solution including these terms will be the subject of future numerical studies. The corresponding coupling matrix elements have a structure similar to those in generalized Anderson models,¹⁴ that will allow to reproduce effects like dynamical anticrossings between two resonant absorption resonances in the conduction and valence subbands. Note that mid-infrared (MIR) picosecond spectroscopy has demonstrated that interband excitons do not play a role in the intersubband absorption of

GaAs/AlGaAs quantum well lasers.¹⁰ Especially for large quantum well widths, the main many-body correction to intersubband optical spectra is the depolarization shift. The presence of an electron hole plasma does not significantly alter the measured dynamic depolarization shift of the electronic intersubband resonance.¹¹ However theoretical studies predict a reduction in oscillator strength for electronic intersubband transitions if the energy of one electron subband approaches the top of the well, and the effected is expected to be of relevance in the design of quantum well devices producing MIR.¹⁵

The presence of holes in the valence bands as well as interband excitons should be more relevant in very small band gap materials, where both interband and some intersubband transition energies are comparable, and could both contribute to the far infrared spectrum. These issues will be addressed in future publications as discussed above, by considering an extended numerical inversion scheme that allows for Coulomb coupling between different transitions.

We obtain optical spectra, by computing exchange with the bare Coulomb interaction. In a formal development, screening appears only in higher-order diagonal and nondiagonal terms beyond Hartree-Fock, and detailed studies including comparisons with experiments indicate that there are strong compensations between diagonal and nondiagonal terms for both intersubband,¹⁶ and interband transitions.¹⁷ A detailed analysis of the interplay of diagonal and nondiagonal contributions in the nonparabolic band-coupling scenario will be the subject of further research. Here we consider a constant dephasing rate, evaluated for each transition using carrier-carrier scattering. More details of the derivation are given in the Appendix.

III. NUMERICAL RESULTS AND DISCUSSION

The numerical results presented here are for four different structures. We start with structures that have been widely studied in the interband case and samples can be easily obtained to attract the interest of experimentalists. They are GaAs/AlGaAs quantum wells with well widths of 5, 10, and 20 nm. Next we choose a structure that has been used for high density interband lasing operation and thus it is reasonable to look for effects that can be seen only at high electron and hole density. It is a 9 nm thick compressively strained InGaAsP QW (E_g unstrained 1.344 eV, $\epsilon = -1.5\%$), embedded in 5 nm tensile-strained GaAsP spacer layers (E_g unstrained 1.826 eV, $\epsilon = 1.2\%$), and in AlGaAs (E_g 1.842 eV). The band offsets were calculated according to model-solid theory.²⁰ We have chosen the QW described above for two reasons: (i) it suits our purposes to demonstrate the band coupling and Coulomb effects. (ii) The design and constituent parameter choice is of technological interest. More details of the sample design can be found in Ref. 21.

After optical excitation, the total density of electrons is equal to that of holes, and the occupation functions are given by Fermi functions, with one chemical potential characterizing all electron subbands and one for all the hole subbands, assumed to be thermalized at $T = 300$ K. Only carrier-carrier scattering is included in our calculations. Before we proceed

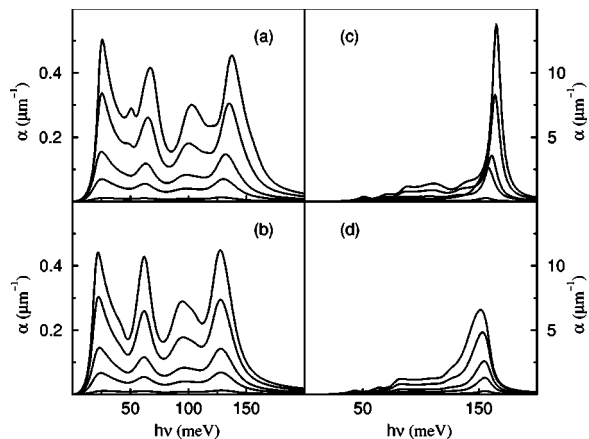


FIG. 1. Intersubband absorption of a 5 nm GaAs/AlGaAs quantum well with contributions from both conduction and valence bands. Many-body effects are included in (a) and (c). Free-carrier spectra are given in (b) and (d). TE polarization on (a) and (b), and TM on (c) and (d). In all panels, from bottom to top, the curves correspond to excitation with a total carrier density $N=0.1, 0.5, 1, 2,$ and $3 \times 10^{12} \text{ cm}^{-2}$.

to discuss numerical results, a brief summary of the numerical method is useful. We start by diagonalizing an $8 \times 8 \mathbf{k} \cdot \mathbf{p}$ Hamiltonian. The $\mathbf{k} \cdot \mathbf{p}$ method uses a Kane-type Hamiltonian operator including the lowest conduction band, the three uppermost valence bands, all are assumed to be Kramers degenerated. No axial approximation and no block diagonalization is applied. The momentum operator is calculated consistently with the Hamilton operator by evaluating the k gradient.¹⁸ For quantum wells, the components of the k -vector parallel to the growth direction are replaced by the corresponding symmetrized spatial derivatives as outlined in Ref. 8. Spurious solutions are eliminated by a proper choice of the interband momentum matrix element P similarly as proposed in Ref. 19, and a rescaling of the momentum operator. Next, for a given carrier density, the equilibrium (Fermi) occupation functions, Coulomb matrix elements [Eq. (3)], dephasing rates [Eq. (A13)] and renormalized energies [Eq. (4)] are evaluated. Equation (A8) is then discretized leading to a system of linear equations which is solved for each photon frequency. A final numerical integration and summation over all possible intersubband transitions yields the final optical spectra [Eq. (1)]. K space is partitioned in sections between 0 and a maximum value K_{max} and the density of k points is doubled until the resulting numerical inversion and integrations converge. A total of either 100 or 200 k points suffices for calculations with temperatures between 200 and 300 K.

Figure 1 compares and contrasts the TE and TM absorption of a 5 nm GaAs/AlGaAs quantum well as a function of increasing carrier density with and without many-body effects. The electrons dominate the TM mode spectra but do not contribute for TE polarization. The number of resolved peaks as the carrier density increases is different with and without many-body effects, which could lead to interesting experimental investigations to test our theory. The main contributions to the TE spectra for $N=3 \times 10^{12} \text{ cm}^{-2}$ are depicted in detail in Fig. 2. The striking feature here is that the struc-

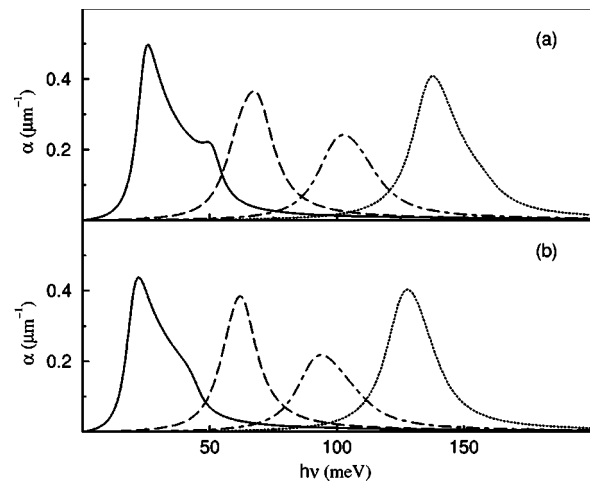


FIG. 2. Main contributions for the TE absorption of the quantum well in Fig. 1. The carrier density is $N=3 \times 10^{12} \text{ cm}^{-2}$. Many-body effects are included in (a). Free-carrier spectra are given in (b). In both panels, from left to right, the solid, long-dashed, dotted-dashed, and dotted lines correspond to the (2,1), (3,2), (4,2), and (4,1) transitions among the valence subbands.

ture that appears around 50 meV is not due to another transition, but rather by a combination of band-structure and many-body effects. The corresponding dipole moment is shown in Fig. 3(c) as a solid line. It starts from zero at $k=0$ evolves quickly to its maximum and falls also quickly to zero. As a consequence, the available k space is restricted and the Coulomb corrections, actually dominated by the depolarization shift do not have strength to promote a full shift of oscillator strength to the high energy side. The band structure for both valence and conduction bands are shown, respectively in Figs. 3 and 4. Note that the TM dipole moments for electrons and those corresponding to the main contribu-

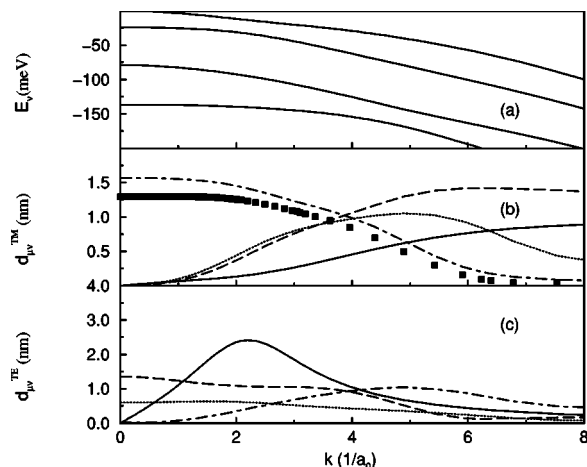


FIG. 3. (a) Valence subbands of the quantum well in Fig. 1. E_{ν} , obtained from the diagonalization of a $8 \times 8 \mathbf{k} \cdot \mathbf{p}$ Hamiltonian. (b) Selected TM transition dipole moments, $d_{\mu\nu}^{\text{TM}}$, within the valence subbands. (c) TE transition dipole moments, $d_{\mu\nu}^{\text{TE}}$. The solid, long-dashed, dotted-dashed, and dotted lines follow the convention of Fig. 2 in (b) and (c). The curve with square symbols in (b) is for the (3,1) transition ($a_0 \approx 8.0 \text{ nm}$).

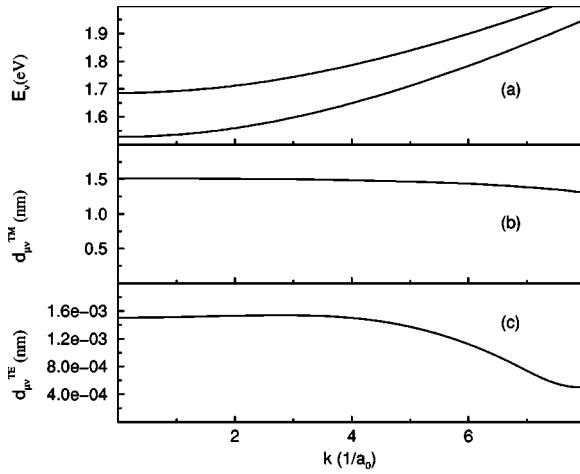


FIG. 4. (a) Conduction subbands of the quantum well in Fig. 1. E_{ν} , obtained from the diagonalization of a $8 \times 8 \mathbf{k} \cdot \mathbf{p}$ Hamiltonian. (b) TM transition dipole moment, $d_{\mu\nu}^{TM}$, within the conduction subbands. (c) TE transition dipole moment, $d_{\mu\nu}^{TE}$ ($a_0 \approx 8.0$ nm).

tions from valence bands show a small variation in the whole region of k space where the subbands are appreciably populated and thus contribute to the spectra. Consequently, the many-body corrections, which manifest in the predicted spectra as spectral shifts and redistribution of oscillator strength are more effective, as shown in a comparison between Figs. 1(c) and 1(d).

Figure 5 is similar to Fig. 1, but for a 10 nm GaAs/AlGaAs quantum well. Selected contributions for both TE and TM modes are shown in Fig. 6.

In the low energy side of the TM mode, dominated by hole transitions the number and shape of well resolved peaks are different for free carriers and many-body spectra. The structure around 67 meV is particularly interesting. It is not present for free carriers and appears in the many-body spectrum as a combination of larger separation between the (4,1)-

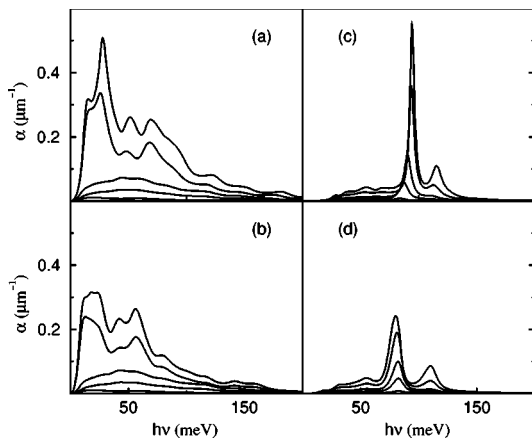


FIG. 5. Intersubband absorption of a 10 nm GaAs/AlGaAs quantum well with contributions from both conduction and valence bands. Many-body effects are included in (a) and (c). Free-carrier spectra are given in (b) and (d). TE polarization on (a) and (b), and TM on (c) and (d). In all panels, from bottom to top, the curves correspond to excitation with a total carrier density $N=0.1, 0.5, 1,$ and $3 \times 10^{12} \text{ cm}^{-2}$.

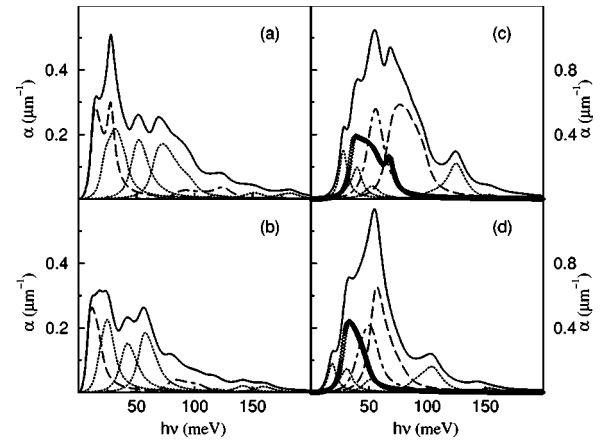


FIG. 6. Main contributions to the absorption due to intervalence band transitions for the quantum well of Fig. 5 excited with a total carrier density $N=3 \times 10^{12} \text{ cm}^{-2}$. Many body effects are included in (a) and (c) and free-carrier curves are shown in (b) and (d). In all panels the solid curves are the total valence subband contribution. For TE polarization, (a) and (b), from left to right the main contributions are (2,1) (3,2) (4,2) (4,1) (7,3) (5,1) (7,2) (7,1). The (2,1) and (5,1) are highlighted by dashed and dotted-dashed curves, respectively. For TM polarization, (c) and (d), from left to right the main contributions are (2,1) (3,1), (3,2) (4,2) (5,3) (4,1) (5,1) (7,2). The (3,1), (4,1), and (4,2) transitions are highlighted by symbols, dashed and dotted-dashed curves, respectively.

dashed and (4,2)-dotted-dashed transitions combined with a double peak that develops in the (3,1)-symbols structure. Also the TE presents an interesting low-energy feature around 16 meV, once more due to a single transition (2,1) that evolves to a double featured one due to many-body effects and the sharply peaked dipole moment, highlighted as a dashed line in Fig. 7(c). The double featured (5,1) transition also contributes to change considerably the spectrum around 90 and 124 meV.

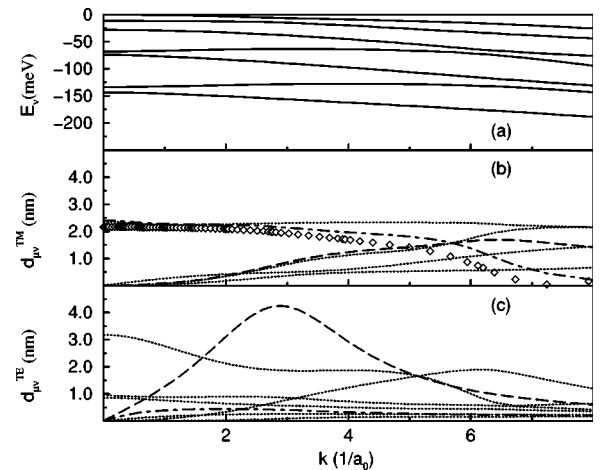


FIG. 7. (a) Valence subbands of the quantum well in Fig. 5. E_{ν} , obtained from the diagonalization of a $8 \times 8 \mathbf{k} \cdot \mathbf{p}$ Hamiltonian. (b) Selected TM transition dipole moments, $d_{\mu\nu}^{TM}$, within the valence subbands. The (3,1), (4,1), and (4,2) transitions are highlighted by symbols, dashed, and dotted-dashed curves, respectively. (c) TE transition dipole moments, $d_{\mu\nu}^{TE}$. The (2,1) and (5,1) are highlighted by dashed and dotted-dashed curves, respectively ($a_0 \approx 8.0$ nm).

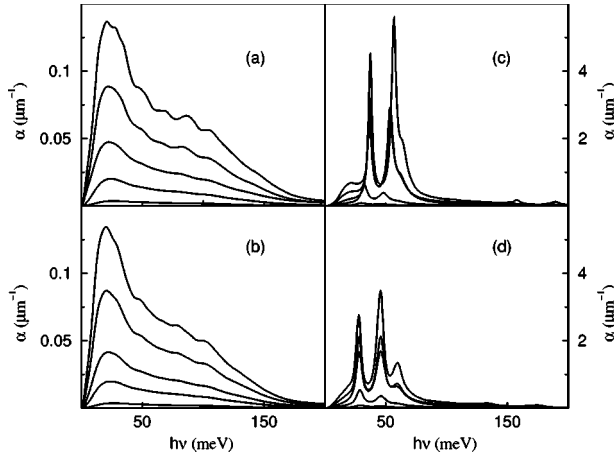


FIG. 8. Intersubband absorption of a 20 nm GaAs/AlGaAs quantum well with contributions from both conduction and valence bands. Many-body effects are included in (a) and (c). Free-carrier spectra are given in (b) and (d). TE polarization on (a) and (b), and TM on (c) and (d). In all panels, from bottom to top, the curves correspond to excitation with a total carrier density $N=0.1, 0.5, 1, 2,$ and $3 \times 10^{12} \text{ cm}^{-2}$.

Strong differences between the number of resolved structures and the relative oscillator strengths for both TE and TM modes are also found for the 20 nm structure, which has however a large number of different transitions contributing to the final spectra, so we skip a detailed analysis and show only the evolution of total spectra with and without many-body effects in Fig. 8.

We now complement the general discussion by analyzing a 9 nm InGaAsP/GaAsP quantum well. Its design and structural parameters are given in detail in Ref. 21.

Probe absorption spectra including contributions from both conduction and valence bands are shown for TM and TE modes, respectively, in Figs. 9 and 10. Valence and conduction subbands as well as selected transition dipole moments are depicted in Figs. 11 and 12.

Direct comparison between dipole moments shows that, as expected the conduction band electrons dominate the TM mode absorption, while the valence bands dominate the TE case. Without coupling between conduction and valence bands, the TE transitions would be forbidden for the conduction subbands. However, the bands are coupled. The coupling gives rise to the structure around 164 meV in Fig. 10(a), which originates from (2,4) and (1,3) transitions. The corresponding dipole moments are, respectively, the solid and long-dashed curves in Fig. 12(c). The Coulomb enhancement is necessary to make the transitions visible. They are not resolved for free-carriers [see Fig. 10(b)].

The conduction bands are parabolic in excellent approximation, but we find that the coupling with the valence band leads to a small dispersion, i.e., from bottom to top, the adjusted effective masses are given by $m_{e,v}=0.106, 0.119, 0.130, 0.127,$ and $0.129 \times m_0$, where m_0 is the free electron mass. The TM dipole moments are roughly constant, and the TE is strongly k dependent, starting from zero at $k=0$. In contrast, the valence bands are strongly coupled, as seen in Fig. 11, and cannot be approximated by parabolic bands.

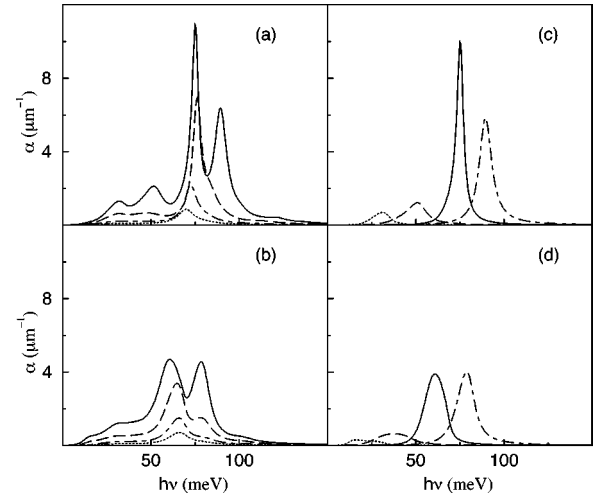


FIG. 9. Intersubband absorption of a 9 nm InGaAsP/GaAsP quantum well including contributions from both conduction and valence bands with TM polarization. Many-body effects are included in (a) and (c). Free-carrier spectra are given in (b) and (d). From bottom to top on (a) and (b), the dotted, dotted-dashed, long-dashed, and solid curves correspond to excitation with a total carrier density $N=0.5, 1, 2.5,$ and $5 \times 10^{12} \text{ cm}^{-2}$. The main contributions to the spectrum with $N=5 \times 10^{12} \text{ cm}^{-2}$ are shown in (c) and (d). From left to right, the dotted, and long-dashed curves are for the (2,1) and (3,2) absorption transitions on the valence subbands. The solid and dotted-dashed curves are for the (1,2) and (2,3) conduction subbands.

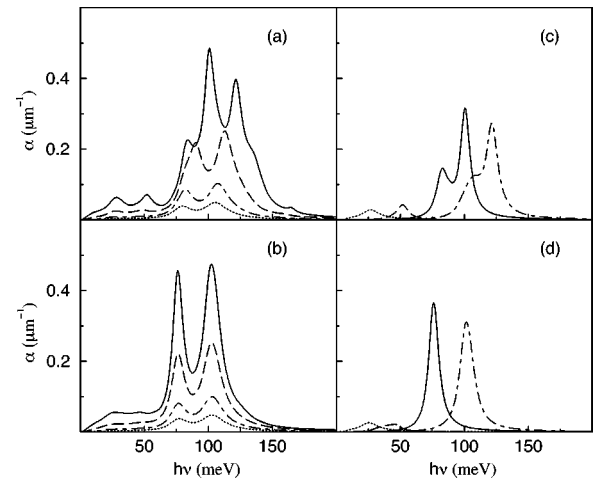


FIG. 10. Intersubband absorption for the quantum well of Fig. 9 including contributions from both conduction and valence bands with TE polarization. Many-body effects are included in (a) and (c). Free-carrier spectra are given in (b) and (d). From bottom to top on (a) and (b), the dotted, dotted-dashed, long-dashed, and solid curves correspond to excitation with a total carrier density $N=0.5, 1, 2.5,$ and $5 \times 10^{12} \text{ cm}^{-2}$. The main contributions to the spectrum with $N=5 \times 10^{12} \text{ cm}^{-2}$ are shown in (c) and (d). From left to right, the dotted, long-dashed, solid, and dotted-dashed curves correspond to absorption between the valence subbands (5,4), (3,2), (4,1), and (5,1).

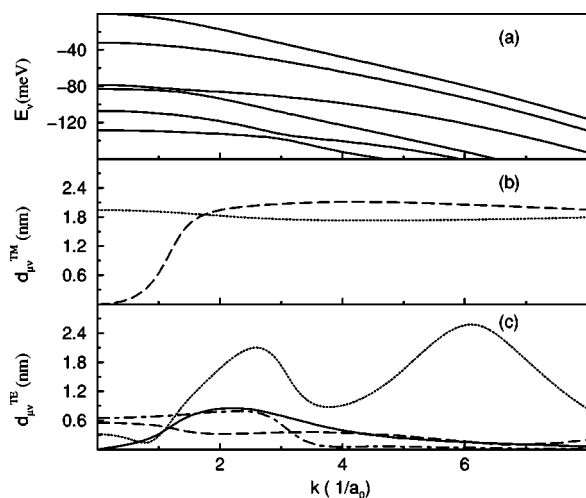


FIG. 11. (a) Valence subbands E_v , obtained from the diagonalization of a $8 \times 8 \mathbf{k} \cdot \mathbf{p}$ Hamiltonian for the 9 nm InGaAsP/GaAsP quantum well of Fig. 9. (b) Selected TM transition dipole moments, $d_{\mu\nu}^{TM}$, within the valence subbands. The dotted and long-dashed lines are for the (2,1) and (3,2) transitions (c) TE transition dipole moments, $d_{\mu\nu}^{TE}$. The dotted, long-dashed, solid, and dotted-dashed curves are for the (5,4) (3,2) (4,1), and (5,1) transitions ($a_0 \approx 8.5$ nm).

Most dipole moments are strongly k dependent on both TM and TE modes. If, just to quantify the amount of band coupling to compare with the conduction bands, we make a parabolic least square fit, the resulting effective masses, from the top valence band read $m_{h,v} = 0.231, 0.307, 0.432, 0.273, 0.322,$ and $0.420 \times m_0$.

The valence contributions (2,1) and (3,2) in the TM mode [respectively, given by the dotted and long-dashed curves in Fig. 9(c)], as well as (5,4) and (3,2) for TE [respectively,

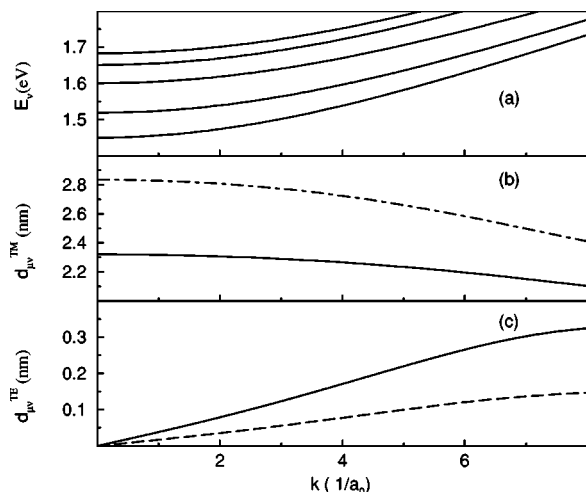


FIG. 12. (a) Conduction subbands of a 9 nm InGaAsP/GaAsP quantum well, E_v , obtained from the diagonalization of a $8 \times 8 \mathbf{k} \cdot \mathbf{p}$ Hamiltonian. (b) Selected TM transition dipole moments, $d_{\mu\nu}^{TM}$ within the conduction subbands. The dotted-dashed and solid lines are, respectively, for the (3,2) and (2,1) transitions. (c) TE transition dipole moments, $d_{\mu\nu}^{TE}$. The solid and long-dashed curves correspond to the (2,4) and (1,3) transitions ($a_0 \approx 8.5$ nm).

given by the dotted and long-dashed curves in Fig. 10(c)] have a similar qualitative behavior. [Corresponding dipole moments are depicted in Figs. 11(b) and 11(c).] In these four cases, there is a strong subband dispersion (measured quantitatively by the different adjusted effective masses), and the transition dipole moments are either roughly constant or evolve quickly to large average value in a sizeable region of k space leading to broad free-carrier absorption.

The different Coulomb contributions can effectively redistribute the oscillator strength of the transitions leading to well-defined peaks. However, the main valence band contributions for the TE mode, (4,1) and (5,1) behave remarkably differently. The dipoles are shown as solid and dotted-dashed curves in Fig. 11(c). The k -space region where the dipole moments are appreciable is restricted, and that leads, even in the free carrier case, to sharper structures. There is consequently not enough k -space available to allow the Coulomb interaction to redistribute the oscillator strength to a single peak. Thus, combining all transitions, which corresponds to an actual optical experiment and analyzing the TE spectrum between 75 and 150 meV, the double-peaked feature evolves to a three-peaked feature as we increase the density by increasing pump density. The extra features are similar in origin to those depicted in Fig. 6, demonstrating that the underlying effect can appear in quantum well systems of different composition and design characteristics, thus increasing the generality of our analysis.

The spectra can be measured experimentally and the different conduction and valence band signatures can be located by comparing and contrasting the evolution of TE and TM absorption with increasing pump density. The extra features are not present in free carrier calculations.

IV. SUMMARY

In summary, the following issues have been addressed in this paper. A pump and probe scheme with optical excitation that eliminates the need for doping in the sample has been proposed to study intersubband transitions. The combined contributions from conduction and valence subbands for the intersubband transitions including many-body effects and nonparabolicity in all subbands has been reported. The evolution of TM and TE modes is remarkably different and extra peaks can appear in the TE spectra due to the Coulomb interaction in the valence bands. Furthermore, resolvable conduction band contributions can be found in the TE spectra due to a combination of band-coupling and Coulomb corrections, also demonstrated here for the first time. Four different structures were analyzed confirming the general trends predicted by our theory: the spectral positions and broadening, number of peaks and the relative oscillator strengths of the spectra calculated with Coulomb effects are remarkably different from the free carrier case, further highlighting the relevance of our calculations.

ACKNOWLEDGMENTS

The authors thank Science Foundation Ireland (SFI) and the Deutsche Forschungsgemeinschaft (DFG) for financial support of this work.

APPENDIX: DYSON EQUATIONS

The excited semiconductor is described by nonequilibrium Green's functions for the interacting quasiparticles, carriers (G) and plasmons (W),

$$i\hbar G(\underline{12}) = \langle \Psi(\underline{1}) \Psi^\dagger(\underline{2}) \rangle, \quad (A1)$$

$$W(\underline{12}) = \frac{\delta \Phi_{\text{eff}}(\underline{1})}{\delta \rho_{\text{ext}}(\underline{2})},$$

where we have used a functional derivative with respect to an external perturbation.¹³

The electric field \vec{E} , which appears later in the text is classical, i.e., we have a semiclassical theory. A fully quantized treatment would have a photon Green's function as well and will be the subject of further investigations. The quantum mechanical averages are calculated along the double-time Keldysh contour, C . Time arguments running along C are underlined, and T_C denotes the time-ordering operator along C . In other words, the notation $\underline{1} = \vec{R}_1, \underline{t}_1$ means that time runs under the contour from $-\infty$ to $+\infty$ on a positive branch, $\underline{t}_1 = t_+$ and back on a negative branch from $+\infty$ to $-\infty$, and thus $\underline{t}_1 = t_-$, e.g., for a given operator \mathcal{M} ,

$$\mathcal{M}_{\text{eff}}(\underline{1}) = \langle \mathcal{M}(\vec{R}_1, \underline{t}_1) \rangle = \frac{\text{tr}\{\rho_0 T_C[\mathcal{M}(\vec{R}_1, \underline{t}_1) S_C]\}}{\text{tr}\{\rho_0 S_C\}},$$

$$S_C = T_C \exp\left(-i \int_C H_{\text{ext}}(t) dt\right). \quad (A2)$$

The Keldysh Green's functions time evolution is described by Dyson equations (sum over repeated arguments is assumed)

$$[G_0^{-1}(\underline{13}) - \Sigma(\underline{13})]G(\underline{32}) = \delta(\underline{12}),$$

$$[W_0^{-1}(\underline{13}) - p(\underline{13})]W(\underline{32}) = \delta(\underline{12}). \quad (A3)$$

The carriers and plasmon self-energy, called for now on, respectively, self-energy and longitudinal polarization function, read

$$\Sigma(\underline{12}) = -i\hbar e G(\underline{13}) W(\underline{41}) \frac{\delta G^{-1}(\underline{32})}{\delta \Phi_{\text{eff}}(\underline{4})},$$

$$p(\underline{12}) = -i\hbar e \frac{\delta G(\underline{11}^+)}{\delta \Phi_{\text{eff}}(\underline{2})}. \quad (A4)$$

The inverse free propagators are given by

$$G_0^{-1}(\underline{13}) = \left[i\hbar \frac{\partial}{\partial t_1} - h_{\text{eff}}(\underline{1}) \right] \delta(\underline{13}),$$

$$W_0^{-1}(\underline{12}) = -\frac{\epsilon_0}{4\pi e^2} \Delta_1 \delta(\underline{12}). \quad (A5)$$

Here ϵ_0 is the static dielectric function. The effective one-particle Hamiltonian in the equation for the free carrier propagator reads

$$h_{\text{eff}}(\underline{1}) = H_0(\underline{1}) + \Phi_{\text{eff}}(\underline{1}) - e\vec{R} \cdot \vec{E}(\underline{1}). \quad (A6)$$

We are interested in the projection onto the $[\nu\mu]$ coupling that yields optical and tunneling transition rates between subbands ν and μ . If an eigenstate is characterized by the subband label ν and k for the quasimomentum corresponding to energy $\hbar\epsilon_\nu(k)$ is denoted $\phi_{\nu k}(R)$, $R \equiv (\vec{r}, z)$,

$$\mathcal{A}_{\nu\mu}(k, t) = \int \phi_{\nu k}^*(R_1) \mathcal{A}(R_1, R_2) \phi_{\mu k}(R_2) dR_1 dR_2. \quad (A7)$$

The equation of motion in the physical limit, $t_1 = t_2 = t$, reads

$$i\hbar \left(\frac{\partial}{\partial t} + i(e_\nu - e_\mu) \right) G_{\nu\mu}^<(k, t) + \vec{\varphi}_{\nu\mu}(k) \cdot \vec{E}(t)$$

$$\times (G_{\mu\mu}^<(k, t) - G_{\nu\nu}^<(k, t)) - i\hbar \mathcal{V} \begin{pmatrix} \nu\mu\mu\nu \\ 0 \end{pmatrix}$$

$$\times (G_{\nu\nu}^<(k, t) - G_{\mu\mu}^<(k, t)) \sum_{\vec{k}'} G_{\nu\mu}^<(k', t) + (G_{\mu\mu}^<(k, t)$$

$$- G_{\nu\nu}^<(k, t)) \sum_{\vec{k}'} G_{\nu\mu}^<(k', t) i\hbar \mathcal{V} \begin{pmatrix} \nu\nu\mu\mu \\ k - k' \end{pmatrix} = I_{\nu\mu}(k, t). \quad (A8)$$

The left-hand side has the Hartree-Fock contribution while the right-hand side has correlation terms, which include, e.g., electron-electron scattering and nondiagonal dephasing. The correlation contribution has a general structure,

$$I_{\nu\mu}(k, t) = \sum_{\lambda} \int_{-\infty}^t [\Sigma_{\nu\lambda}^<(k, tt') G_{\lambda\mu}^>(k, t't) + G_{\nu\lambda}^>(k, tt') \Sigma_{\lambda\nu}^<(k, t't)$$

$$- (> \Leftrightarrow <)]. \quad (A9)$$

In what follows, we make the GW approximation for the self-energy, i.e.,

$$\Sigma^{\cong}(\underline{12}) = i\hbar W^{\cong}(\underline{12}) G^{\cong}(\underline{12}). \quad (A10)$$

Furthermore, we assume that the carriers reach steady-state (although in principle still out of equilibrium) while the microscopic polarization is still evolving. Thus, in Eq. (A8), we can write the diagonal terms like $G_{\mu\mu}^<(k, t)$ simply as $G_{\mu\mu}^<(k)$. At this point, we can simplify the notation by introducing occupation functions $f_\lambda = -i\hbar G_{\lambda\lambda}^<(k)$, and microscopic polarizations $p_{\nu\mu}(k, \omega)$, $-i\hbar G_{\nu\mu}^<(k, \omega)$, or equivalently, optical susceptibilities, $\chi_{\nu\mu}(k, \omega) = p_{\nu\mu}(k, \omega)/E_0$.

Only representative projection terms will be kept, since solving the equations using the full Coulomb couplings that originate from the projections is at present beyond our current numerical capability. We separate the contributions into a number of diagonal (subscript d), and nondiagonal (subscript nd) contributions,

$$I_{\nu\mu}(k, t) = I_d^{\nu\nu\nu\nu}(k, t) + I_d^{\mu\mu\mu\mu}(k, t) + I_{nd}^{\nu\nu\mu\mu}(k, t) + I_{nd}^{\mu\mu\nu\nu}(k, t)$$

$$+ I_d^{\nu\nu\mu\nu}(k, t) + I_d^{\mu\nu\nu\mu}(k, t) + I_{nd}^{\mu\nu\mu\nu}(k, t) + I_{nd}^{\mu\nu\nu\mu}(k, t). \quad (A11)$$

After Fourier transforming Eq. (A8), and keeping only the first two diagonal terms in Eq. (A11), we obtain

$$I_{\nu\mu}(k, \omega) = -iG_{\nu\mu}^<(k, \omega) \sum_{\vec{q}} \Gamma_{\nu\mu}(k, q, \omega), \quad (\text{A12})$$

which can be further simplified by evaluation at $k=0$ and $\omega=e_\lambda(0)$. In other words, we approximate the dephasing mechanisms by a constant carrier-carrier scattering rate.

$$I_{\nu\mu}(k, \omega) = -i\Gamma_{\nu\mu} G_{\nu\mu}^<(k, \omega),$$

$$\Gamma_{\nu\mu} = -\mathcal{J}[\sum_{\nu\nu'}^r(0, e_\nu(0)) + \sum_{\mu\mu'}^r(0, e_\mu(0))],$$

$$\sum_{\vec{q}, \vec{q}'}^r(k, \omega) = \sum_{\vec{q}, \vec{q}'} \left| W^r \begin{pmatrix} \nu\nu\nu\nu \\ q \end{pmatrix} \right|^2 \times \frac{\mathcal{F}_\nu(k, q, q')}{\omega - e_\nu(k-q) - e_\nu(q+q') + e_\nu(q') + i\gamma},$$

$$\mathcal{F}_\nu(k, q, q') = f_\nu(k+q)f_\nu(q+q')(1-f_\nu(q')) + (1-f_\nu(k+q)) \times (1-f_\nu(q+q')f_\nu(q')), \quad (\text{A13})$$

where we have the static single plasmon pole screened potential, and actually take the limit $\gamma \rightarrow 0$. Equation (2) in the main part of this paper is thus obtained from the Fourier transform of Eq. (A8) using Eq. (A13).

-
- ¹D. C. Larrabee, G. A. Khodaparast, J. Kono, K. Ueda, Y. Kakajima, S. Sasa, M. Inoue, K. I. Kolokolov, J. Li, and C. Z. Ning, *Appl. Phys. Lett.* **83**, 3936 (2003).
- ²S. Tsujino, M. Rüfenacht, H. Nakajima, T. Noda, C. Metzner, and H. Sakaki, *Phys. Rev. B* **62**, 1560 (2000).
- ³S. Luin, V. Pellegrini, F. Beltram, X. Marcadet, and C. Sirtori, *Phys. Rev. B* **64**, 041306 (2001).
- ⁴H. C. Liu and A. J. Spring *Phys. Rev. B* **61**, 15 629 (2000).
- ⁵D. E. Nikonov, A. Imamoglu, L. V. Butov, and H. Schmidt, *Phys. Rev. Lett.* **79**, 4633 (1997).
- ⁶J. Li and C. Z. Ning, *Phys. Rev. Lett.* **91**, 097401 (2003).
- ⁷F. Szmulowicz, *Phys. Rev. B* **51**, 1613 (1995).
- ⁸H. Wenzel, G. Erbert, and P. Enders, *IEEE J. Sel. Top. Quantum Electron.* **5**, 637 (1999).
- ⁹J. R. Hoff, M. Razeghi, and G. J. Brown, *Phys. Rev. B* **54**, 10 773 (1996).
- ¹⁰I. Shtrichman, U. Mizrahi, D. Gershoni, E. Ehrenfreund, K. D. Maranowski, and A. C. Gossard, *Appl. Phys. Lett.* **76**, 2988 (2000).
- ¹¹I. Shtrichman, C. Metzner, E. Ehrenfreund, D. Gershoni, K. D. Maranowski, and A. C. Gossard, *Phys. Rev. B* **65**, 035310 (2001).
- ¹²L. V. Keldysh, *Zh. Eksp. Teor. Fiz.* **20**, 4 (1965) [*Sov. Phys. JETP* **20**, 4 (1965)].
- ¹³M. F. Pereira, Jr. and K. Henneberger, *Phys. Rev. B* **58**, 2064 (1998).
- ¹⁴P. W. Anderson, *Phys. Rev.* **124**, 41 (1961).
- ¹⁵A. Mizel, I. Shtrichman, and D. Gershoni, *Phys. Rev. B* **65**, 235313 (2002).
- ¹⁶I. Waldmüller, M. Woerner, J. Förstner, and A. Knorr, *Phys. Status Solidi B* **238**, 474 (2003).
- ¹⁷G. Manzke, Q. Y. Peng, K. Henneberger, U. Neukirch, K. Hauke, K. Wundke, J. Gutowski, and D. Hommel, *Phys. Rev. Lett.* **80**, 4943 (1998).
- ¹⁸P. Enders, A. Barwolff, M. Woerner, and D. Suiskey, *Phys. Rev. B* **51**, 16 695 (1995).
- ¹⁹B. A. Foreman, *Phys. Rev. B* **56**, R12748 (1997).
- ²⁰C. G. Van de Walle, *Phys. Rev. B* **39**, 1871 (1989).
- ²¹G. Erbert, F. Bugge, A. Knauer, J. Maege, A. Oster, J. Sebastian, R. Staske, A. Thies, H. Wenzel, M. Weyers, and G. Traenkle, *Proc. SPIE* **3628**, 19 (1999).